JOURNAL OF AIRCRAFT
Vol. 47, No. 2, March–April 2010

Planform and Camber Effects on the Aerodynamics of Low-Reynolds-Number Wings

Taylor Swanson*
Arnold Engineering Development Center, Arnold Air Force Base, Tennessee 37389
and
K. M. Isaac†
Missouri University of Science & Technology, Rolla, Missouri 65409

DOI: 10.2514/1.45921

This work is a computational study of the aerodynamics of a wing in a constant freestream at angles of attack ranging from 0 to 45° and an extremely low Reynolds number of 500. Four wings were studied: rectangular with and without camber and semi-ellipse with and without camber. Lift and drag coefficients were determined and their trends were explained, including a lift coefficient peak at ∼20° for all geometries investigated. Flow features were also identified and explained. The dominant flow feature was the tip vortex, which moves streamlines rootward and forms a spiral vortex at high angles of attack for rectangular wings. Semi-ellipse wings also have a spiral vortex at higher angles of attack. Surface stream traces were also investigated and showed complex vortex-dominated flow patterns that depended on planform shape and angle of attack.

I. Introduction

AN INCREASING number of studies on low-Reynolds-number Re_c, high-angle-of-attack α flow is presently underway to support fixed-wing and flapping-wing micro air vehicle (MAV) and nano air vehicle development. Our numerical work on airfoils [1] and experimental work on flapping wings [2,3] has revealed many interesting aspects of the low-Re_c, high-α flow regime. Concepts such as frequency tuning and leading-edge/trailing-edge switching have been proposed as a means of increasing aerodynamic performance and later confirmed by our own results and those of other workers. Trailing-edge vortex trapping is another mechanism that we have proposed in order to augment the lift force on the wing.

The term *low Reynolds number* Re_c is taken to mean less than 4×10^6 in the aerospace literature, which is substantially higher than the $Re_c = 500$ in this study. Re_c is the Reynolds number based on chord length. McMasters and Henderson [4] discussed three Reynolds number modes: subcritical for $Re_c < 400,000$, critical for $400,000 < Re_c < 500,000$, and supercritical for $Re_c > 500,000$. The dominant flow feature in low-Reynolds-number wings is the laminar separation bubble and is discussed by Lissaman [5] and Carmichael [6]. This bubble forms due to the inability of a laminar boundary layer to overcome an adverse pressure gradient, thus forcing it to separate. Once separated, it forms a free shear layer and is more susceptible to transition. After transitioning to turbulent flow, it then reattaches to the surface of the wing as a turbulent boundary layer. If the Reynolds number is less than approximately 50,000, there is insufficient distance for this reattachment. This bubble increases the drag and reduces the performance of the airfoil. Increasing the Reynolds number shrinks the bubble and increases the lift/drag ratio, as in Selig [7].

Little information is available in the literature in the Reynolds number range from 0–1000, but many studies of airfoils in the range from 10,000 to 1×10^6 are available. Laitone [8,9] experimentally investigated cambered-plate wings at Reynolds numbers as low as 20,000. Cambered-plate wings with sharp leading edges were found to give higher lift/drag ratios than with a NACA 0012 section wing. Kunz and Kroo [10] conducted numerical simulations of the two-dimensional Navier–Stokes equations at Re_c below 10,000 to study the effects of camber, thickness, and leading-edge and trailing-edge shapes. In this Re_c range, the maximum lift coefficient was found to increase with decreasing Re_c. However, the lift/drag ratio decreased with decreasing Re_c. They noted the large drag and low lift/drag ratios that are orders of magnitude different from high-Reynolds-number results.

Selig [7] provided an overview of the aerodynamics and design considerations appropriate for this Reynolds number regime, which are a convex pressure recovery, lack of large adverse pressure gradients near the trailing edge, and a transition point that moves forward as angle of attack increases. Force hysteresis at low Reynolds numbers was investigated by Mueller [11] at Reynolds numbers below 300,000, and Selig et al. [12] discussed nonlinear lift and lift hysteresis in wings at Reynolds numbers from 40,000 to 150,000. Both of these effects are attributable to the movement and growth of the laminar separation bubble. As angle of attack increases, the upper-surface bubble grows, thereby increasing displacement thickness and introducing negative camber, and the separation point moves toward the leading edge. At sufficiently high angles of attack, reattachment is impossible and the bubble bursts; this is stall. The process is not symmetric as angle of attack decreases, resulting in hysteresis. Tripping the boundary layer would mitigate some of these effects and would result in a bubble that shrinks and moves upstream as α increases. Biber et al. [13] designed such an airfoil at $Re_c = 50,000$.

Hsiao et al. [14] conducted flow visualization of tip vortices on low-aspect-ratio, rectangular planform, symmetric wings at $Re_c = 100,000$. Lift generated by the suction region caused by these vortices dominated the lift production at high angle of attack: greater than 10°. Tip vortices prove to be beneficial by promoting flow attachment along the upper surface, thereby delaying stall. However, this effect is only present in low-aspect-ratio wings. The effect of a tip vortex is only felt in the immediate vicinity for aspect ratios of eight and larger, according to experiments by Abtahi and Marchman [15] on a cambered rectangular wing with Eppler FX-63-137-ESM cross section at Reynolds numbers from 70,000 to 300,000. However, Viieru et al. [16] found that the tip vortex also poses a hindrance to a specially designed low-Reynolds-number wing for a MAV, in that its downwash reduces the effective angle of attack and causes induced

Presented as Paper 0421 at the 46th AIAA Aerospace Sciences Meeting and Exhibit, Reno, NV, 7–10 January 2008; received 9 June 2009; revision received 22 November 2009; accepted for publication 24 November 2009.

*Aerospace Engineer; Taylor.Swanson@arnold.af.mil. Member AIAA.
†Professor, Aerospace Engineering, 271 Toomey Hall; isaac@mst.edu. Associate Fellow AIAA

drag. Kwon and Park [17] investigated flow features behind an elliptic airfoil and their affect on forces. As α increases, the separation point on the suction surface remains stationary, whereas that on the pressure surface moves aft. Asymmetric flow separation at the trailing edge causes a high lift-curve slope at low angle of attack at $Re_c = 300,000$. In a study by Ricci and Montelpare [18] performed on a cambered airfoil at $Re_c = 200,000$, the separation point was found to be stationary only in a range of α around 2°. Generally, as α increases, the separation point, transition point, and turbulent reattachment point all move toward the leading edge, and the bubble shrinks. A 10%-thick cambered airfoil at $Re_c = 50,000$ was successfully designed by Biber et al. [13] with the gentle stall caused by the shrinking bubble that moves toward the leading edge as α increases.

The effects of camber and planform on flow features and force generation in a low-Reynolds-number flow have been studied by Pelletier and Mueller [19] and by Kaplan et al. [20]. For thin wings, camber was found to be beneficial in the range of Reynolds number from 60,000 to 200,000 [19]. This was attributed to increased tendency toward flow attachment. Planform shape and Reynolds number were found to not affect the lift-curve slope, despite differing wake structures at Reynolds numbers of 8000 and 24,000 [20]. A semi-ellipse wing has a less coherent trailing vortex structure than a rectangular wing [20]. Similarly, at a similar Reynolds number (200,000) and aspect ratio (0.5 to 2), Cosyn and Vierendeels [21] found cambered plates and flat plates to have similar lift characteristics. Drag was also similar until flow over the flat-plate separates.

II. Simulation Details

The present work is a continuation of this ongoing effort in our laboratory to understand the many aspects of low-Re_c, high-α unsteady flow and to use that information for designing and developing micro air vehicles. It has become clear that a systematic study of this problem is essential to make significant progress toward gaining insight into this flow regime. This paper investigates the aerodynamics of a fixed wing, and flapping and plunging wings are investigated elsewhere, in Swanson and Isaac [22]. A problem of this complex nature is best tackled by using all the available tools, which include experiments, computational fluid dynamics (CFD) simulations and analytical approaches. None of these by themselves have the ability to provide all the answers.

Guided by insect wing geometries, in this paper we examined the effects of angle of attack and camber and planform shape on the aerodynamic aspects of thin wings of uniform thickness. Many experimental and CFD studies on conventional airfoils and elliptic cross-sectional airfoils can be found in the literature. However, based on observations of insect wings, a thin platelike airfoil with sharp leading and trailing edges is likely to yield better aerodynamic performance for low-Re_c, high-α flight.

A. Wing Geometry and Solver Overview

Four wings were investigated here. Two have a rectangular planform, one without camber and one with camber. The other two have a semi-elliptical planform, one without camber and one with camber. All four wings have the same span, chord, and thickness, and the two cambered wings have circular arc sections and the same amount of camber. The geometric parameters for the wings are 15 cm span, 5 cm chord, 0.05 cm thickness, and 0.125 cm maximum camber. This is shown in Fig. 1, which also shows the wing orientation convention used herein, except where otherwise noted. The wing tip is to the left, the root is to the right, and the leading edge is above the trailing edge. The aspect ratio is 3.0 for the rectangular wings and 3.82 for the semi-ellipse wings. The wings are not swept, and they have sharp leading and trailing edges. These wings were placed in a hemispherical computational domain consisting of a small hemisphere with 20 cm radius and higher grid density inside a larger hemisphere with 80 cm radius and lower grid density. The base plane of the computational domain is specified as a symmetry plane.

Grids were generated for all four wings to be as similar as possible. From a triangular surface mesh, the volumes were meshed using tetrahedrons. Approximately 850,000 to 920,000 cells resulted for all four wings. The grids were of high quality and results were grid-independent. A grid with 50% more cells altered the resultant force by less than 1%. Also, single-precision and first-order algorithm were found to be satisfactory. The computational domain appears in Figs. 2 and 3, showing the inflow and outflow surfaces and symmetry plane. The cambered semi-ellipse-wing mesh appears in Fig. 4, and the cambered rectangular-wing mesh appears in Fig. 5. Chord is in the x direction, span is in the y direction, and camber is in the z direction. The x–z plane is a symmetry plane. Freestream flow is in the x direction. One-half of the hemispherical surface is set to be inflow and the other half is outflow.

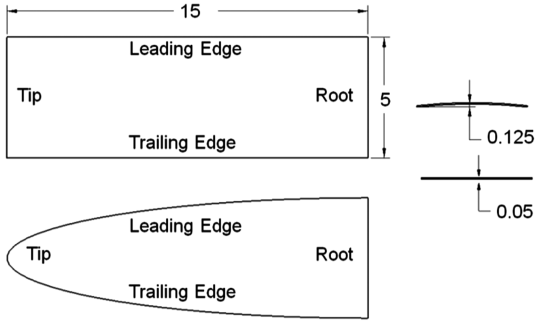

Fig. 1 Wing planforms (left) and profiles (right,) showing 0.125 cm camber and 0.05 cm thickness.

The results presented in this paper were obtained from simulations using the flow solver FLUENT [23]. The main features of the flow solver have been described in [1]. We have established that the present low-Reynolds-number flow is laminar and can be resolved with the mesh size and distribution chosen for this study. Transition does not occur until $Re_c = \mathcal{O}(10^4)$. Young et al. [24] conducted a

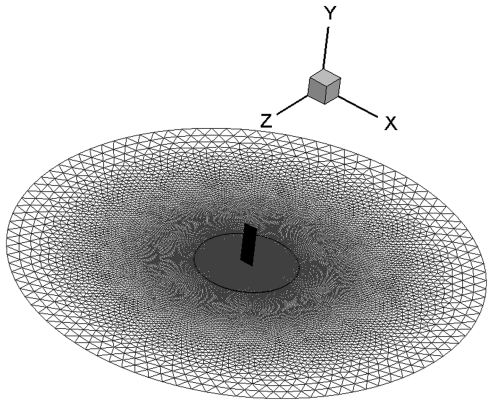

Fig. 2 Cross section of computational domain, showing the wing and circular base surfaces.

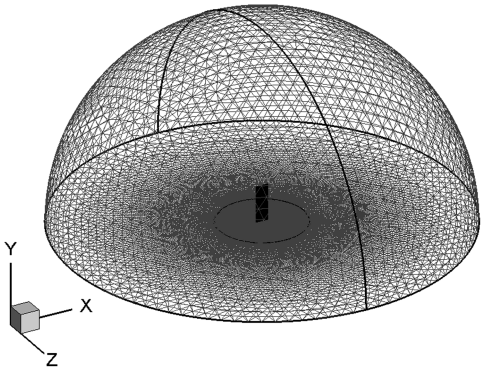

Fig. 3 Hemispherical computational domain, showing the wing and circular base surfaces. The circular arc divides the hemispherical surface into inflow and outflow boundaries.

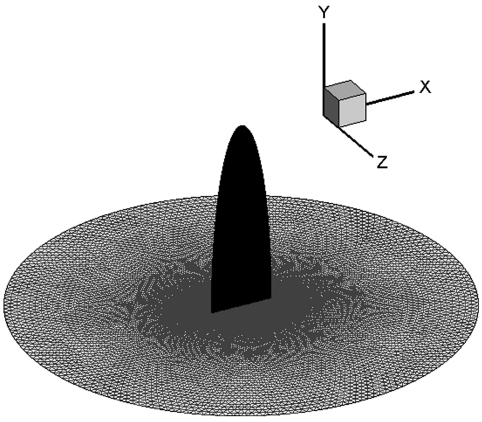

Fig. 4 Semi-ellipse cambered wing and inner portion of meshed symmetry boundary.

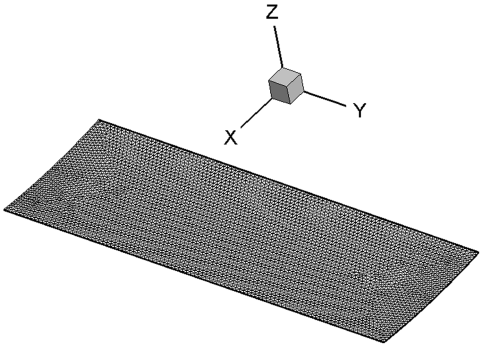

Fig. 5 Triangular mesh on rectangular cambered wing.

dynamic mesh study of a dragonfly wing at Reynolds numbers ranging from 100 to 50,000 and found laminar flow simulations to be sufficient, since the separation point is fixed to the sharp leading edge. In a 2-D computational study that included NACA airfoils, Kunz and Kroo [10] employed a steady laminar technique. However, they noted that the steady assumption degrades convergence at the lowest Reynolds number they covered (namely, 1000), where trailing-edge separation occurs. The residuals and force coefficients were carefully monitored during the runs to determine the number of time steps to be used. The presented results are for flow times of approximately 50 s, which was found to be sufficient for the solution to reach either steady state at lower angles of attack or quasi-steady state at higher angles of attack. Figure 6 illustrates the quasi-steady nature of the force generation. Forces typically begin quite high and then settle into a pattern similar to that shown below, where forces fluctuate due to vortex shedding. All data in Figs. 7–20 were taken

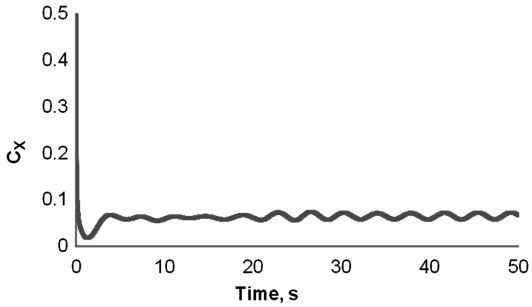

Fig. 6 Quasi-steady force development for rectangular wing with no camber at $Re_c = 500$ and $\alpha = 45°$.

at a peak in this cycle, for consistency. The frequency of these oscillations ranges from 0.34 Hz at $\alpha = 35°$ to 0.26 Hz at $\alpha = 45°$, with a typical amplitude of 0.02.

Our computational technique has been validated by comparison with two-dimensional cylinder flow and two data sets. From a correlation provided in White [25], drag coefficient for a sphere at $Re_c = 500$ is $C_D = 1.16$. Our computed value is $C_D = 1.17$, an excellent agreement. The first data set is from the 3-D experimental study of Sunada et al. [26], in which a flat rectangular wing of aspect ratio of 7 was dragged through a water tank at $Re_c = 4,000$. Experimental errors are well addressed in that paper, and its authors state errors in lift and drag coefficients of less than 8%. The other set is from the 2-D computational work of Kunz and Kroo [10], in which the drag polar for a NACA 0002 airfoil at $Re_c = 1000$ was presented. The results extracted from the above references are accurate to two significant digits. Computed results were generated using the procedure described above, and comparison is shown in Tables 1 and 2. Agreement is generally good, and agreement is better for drag than for lift. Discrepancies are attributed to minor differences in grid generation between our simulations and those of Kunz and Kroo [10], and the use of the steady-flow assumption when comparing our simulations with the experimental data of Sunada et al. [26]. Those problems will not arise in the results presented in Sec. III, since a grid study was conducted and the unsteady-flow solver was used.

III. Results and Discussion

Force data, flow features, and surface stream traces were investigated in this study, and they will be discussed in that order in this section.

A. Force Production

Figure 7 is a drag polar and shows lift and drag coefficients as functions of α for all four wings. It may be clearer to determine trends in those coefficients when plotted directly against angle of attack, as in Figs. 8 and 9. To facilitate clearer discussion, the zero-lift angles of

Table 1 Comparison with Sunada et al. [26]

	C_L			C_D		
α, °	Sunada et al. [26]	Computed	% difference	Sunada et al. [26]	Computed	% difference
15	0.87	0.84	3.4	0.28	0.29	3.6
20	0.90	0.90	0	0.37	0.38	2.7

Table 2 Comparison with Kunz and Kroo [10]

	C_L			C_D		
α, °	Kunz and Kroo [11]	Computed	% difference	Kunz and Kroo [11]	Computed	% difference
0	0.00	0.00	0	0.10	0.10	0
2	0.18	0.17	5.6	0.10	0.10	0
4	0.34	0.30	12	0.11	0.11	0
8	0.55	0.53	3.6	0.13	0.13	0

attack for the cambered wings have been calculated by linear extrapolation, and their values are $-1.76°$ for the rectangular planform wing and $-1.45°$ for the elliptic planform wing, respectively. Linear extrapolation is justified since the lift curve can be seen to be linear for small values of the angle of attack (Fig. 8). Moment coefficient about the quarter-chord, $C_{M,c/4}$, is plotted in Fig. 10. Lift coefficient peaks at 20° for all wings except the noncambered rectangular wing, which peaks at 40°. A lift peak at 20° has been postulated in previous work [1–3] as the angle at which vortices shed, thus explaining the lift peak at that angle. After the peak at $\alpha = 20°$, lift then decreases at $\alpha = 30°$. However, the behavior then differs for the different wings. For the two ellipses, C_L continues to decrease, but the rectangular wings show a lift increase from $\alpha = 30$ to 40° and then a decrease beyond $\alpha = 40°$. It is notable that there is more similarity in behavior between wings of the same planform than between wings that are either both cambered or both flat plates. This indicates that planform shape is more dominant than camber for the wings considered in this study.

There are two possible explanations for the force peak visible in the drag polar and subsequent behavior. First, vortex shedding occurs at the angle of attack corresponding to the force peak and causes additional lift. At higher angles, the vortices have already shed and no longer contribute to lift. The second possible explanation is similar to that of Selig et al. [12] and involves the laminar separation bubble. A large laminar separation bubble exists on airfoils at low Reynolds numbers and high angles of attack. This causes the resultant force vector, which is nearly perpendicular to the wing at low Reynolds numbers, to tilt aft as α increases. The vertical component of that vector will then decrease, as the horizontal component will increase. As α increases, the laminar separation bubble moves toward the leading edge and grows larger. This would increase lift and also drag. At a certain angle of attack, the bubble bursts, causing stall. As α increases beyond this value, the lift coefficient would decrease.

Some other notable, yet predictable, features were observed from the drag polar. The effect of camber is to provide both more lift and more drag at the same angle of attack; the zero-lift point is shifted. Thus, the C_L peak for the cambered wing is greater than that for the noncambered wing. Also as expected, cambered wings develop lift even at $\alpha = 0°$.

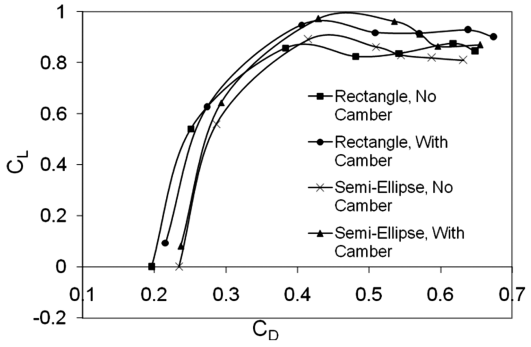

Fig. 7 Drag polar for noncambered and cambered rectangular wings. $Re_c = 500$.

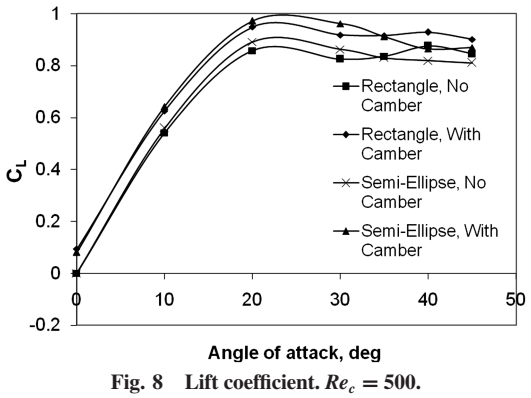

Fig. 8 Lift coefficient. $Re_c = 500$.

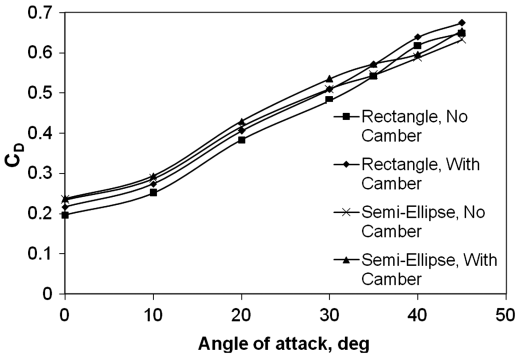

Fig. 9 Drag coefficient. $Re_c = 500$.

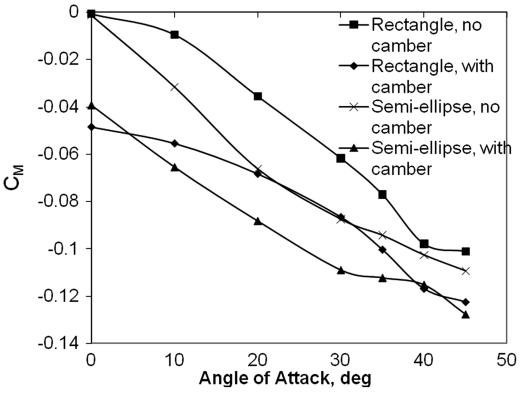

Fig. 10 Moment coefficient about the quarter-chord; $Re_c = 500$.

For comparing the present results, the lowest Reynolds number the authors found in the literature is 1000, at which Kunz and Kroo [10] investigated airfoils. Their study was two-dimensional and was conducted at lower angles of attack than investigated here for our 3-D wings, so additional 2-D cases were run at $Re_c = 500$. Lift coefficient is smaller and drag coefficient is larger at $Re_c = 500$ than at $Re_c = 1000$, as expected. For example, at $\alpha = 0°$, Kunz and Kroo [10] reported $C_D = 0.0998$, and the value we computed for a 2-D airfoil of the same chord and thickness as the wings in this study is $C_D = 0.162$. Similarly, C_L at $\alpha = 8°$ is 0.553 at $Re_c = 1000$ [10], but $C_L = 0.523$ at $Re_c = 500$. Table 3 shows force data for the noncambered rectangular wing at $Re_c = 500$ and 5000 for two angles of attack: 0 and 45°. From the table, it is apparent that the lift and drag coefficients are higher at lower Reynolds numbers.

The pressure distribution that determines moment is provided in Fig. 11 for a flat plate with the same chord and thickness as the 3-D rectangular planform wing with no camber. Figure 12 shows two-dimensional (airfoil) cases for comparison with C_m vs α for the four wings, as previously shown in Fig. 10, including a flat plate and a NACA airfoil at $Re_c = 500$ and a circular arc airfoil at $Re_c = 1000$. C_m values for the circular arc airfoil for $Re_c = 1000$ can be directly compared with the conventional NACA airfoils. The trend is very similar to conventional airfoils: namely, nearly constant value for smaller values of α, and then C_m decreasing for larger values of α. The constant-C_m value is about -0.09 for the $Re_c = 1000$ case, compared with -0.04 for the NACA 2412 airfoil. The larger magnitudes of the moment coefficient for the present $Re_c = 1000$ case may be attributed to the differences in camber, thickness, and Reynolds number. The four curves previously discussed in Fig. 10 are for finite-aspect-ratio wings. The main difference that these have from the airfoils in Fig. 12 is that the C_m curves for the wings in Fig. 10 show a significant negative slope starting at $\alpha = 0$. This is most probably attributable to planform effects, since significant differences are also seen between the rectangular and elliptical planforms. The decrease in moment coefficient at large-α values can

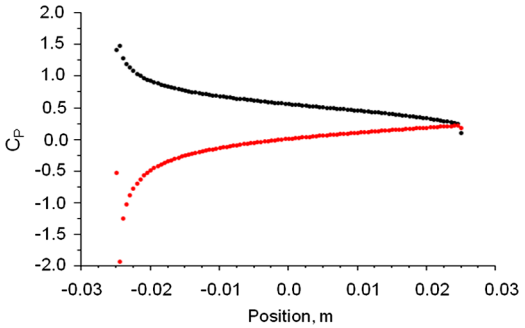

Fig. 11 Pressure distribution for a flat-plate airfoil at $Re_c = 500$ and $\alpha = 10°$; suction surface (lower curve) and pressure surface (upper curve).

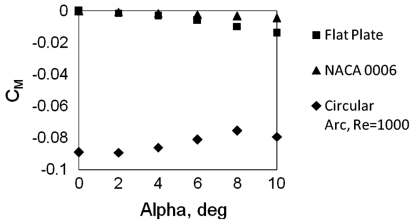

Fig. 12 Moment coefficient about quarter-chord, two-dimensional, $Re_c = 500$ except where noted.

be attributed to stall, since moment coefficient usually decreases after stall; low-Reynolds-number effects might also augment this behavior.

B. Flow Features

The following figures show streamlines for flow over the four wings studied here. Some trends are present for all wings, and there are some features apparent in only one of the wings; these flow features are discussed below. Figures 13–15 show a top view of the flow over the wings at seven angles of attack: 0, 10, 20, 30, 35, 40, and 45° (labeled a—g, respectively). Figures 13 and 14 are for the rectangular wings, without and with camber, respectively, and Figs. 14 and 15 are their semi-ellipse counterparts. Figure 17 shows all four wings at $\alpha = 40°$. Corresponding streamline patterns in Figs. 13 and 14 for the rectangular wings and in Figs. 15 and 16 for the semi-ellipse wings can be used to discuss the effect of camber on the flowfield. They bear substantial similarities, indicating that the qualitative effect of this amount of camber on the flow features is small. At $\alpha = 0°$ without camber (Figs. 13a and 15a) the streamlines do not show any perceptible change in the view shown and are only slightly disturbed with camber (Figs. 14a and 16a). Streamlines proceed straight aft of the wing without any spanwise curvature. At $\alpha = 10°$ (Figs. 13b and 16b), only a minor tip vortex is present, but it starts to become prominent at $\alpha = 20°$ (Figs. 13c and 16c). As α increases beyond this, the tip vortex becomes steadily more prominent. This is revealed as a curvature in the streamline sheet aft of the wing tip. Figures 13c and 13d without camber and Figs. 14c and 14d with camber show streamline curvature at the root of the wing near the symmetry plane. With camber, a spiral vortex originates from the root. Angles of attack of 30° and higher reveal substantial vortices that dominate large portions of the flow. Above 35°, a spiral vortex is formed on every wing but the cambered rectangular wing. A spiral vortex did not form on this wing until 40°.

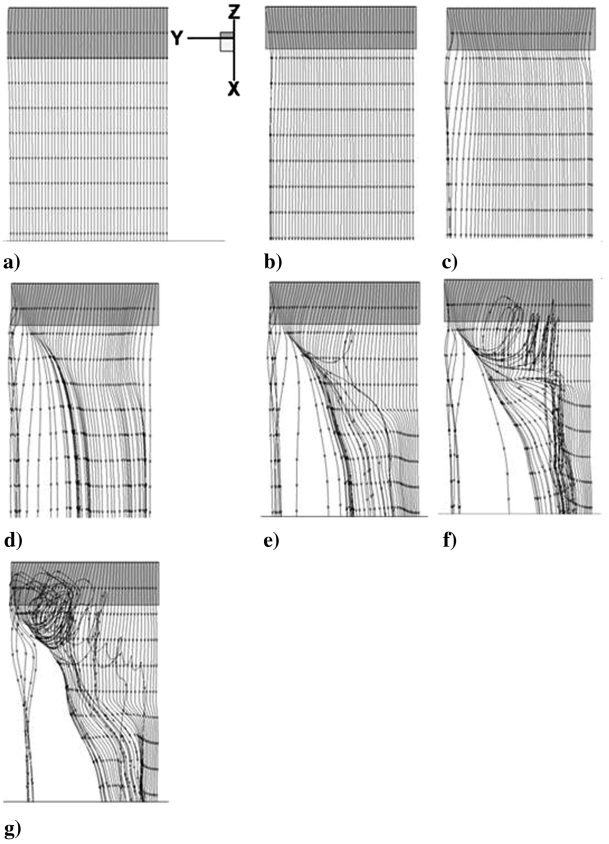

Fig. 13 Streamlines for noncambered rectangular wing viewed from top along a direction between the x and z axes. Axis is for orientation purposes. Flow is from top to bottom, tip is left and root is right. Beginning at the top left, $\alpha = 10$, 10, 20, 30, 35, 40, and 45°. Vortex formation begins at tip and grows as α increases.

Thus, camber appears to enhance flow attachment and delay development of that vortex.

In the spiral vortex, flow is directed against the freestream for a portion of the spiral; this is reversed flow. The spiral vortex forms from the tip in both of the rectangular wings at the applicable angles of attack and in the noncambered semi-ellipse wing at 45°. However, it forms from the root in the noncambered semi-ellipse wing at $\alpha = 35$ and 40° and in the cambered semi-ellipse wing at $\alpha = 35$, 40, and 45°. This could indicate transverse flow from root to tip. Figure 17 shows the different vortex locations for all four wings at $\alpha = 40°$. It is noteworthy that the cambered semi-ellipse wing does not have a spiral vortex at $\alpha = 45°$. An explanation for this is not immediately apparent.

Flow features we referred to as dead-fluid regions [27], regions with few or no streamlines, also appear at and above 35°. The dead-fluid region at 45° extends for a substantial portion of the wing span. Computational particles released from the points used to create these images do not go through those regions, but streamlines originating from other areas do traverse these regions, as in Fig. 18. These low-speed regions with highly-three-dimensional flow features are caused by the tip vortex lifting streamlines up above the wing and transporting them rootward. This is also responsible for compressing many of the streamlines against the symmetry plane. This indicates that for the present fixed-wing cases, substantial spanwise flow is present toward the symmetry plane at higher angles of attack. Also present in Fig. 18 is a flow feature just aft of

Table 3 Coefficient comparison for rectangular wing with no camber at $Re_c = 500$ and $Re_c = 5000$.

Re_c	$\alpha = 0°$			$\alpha = 45°$		
500	$C_L = 0.000$	$C_D = 0.196$	$C_M = -0.001$	$C_L = 0.845$	$C_D = 0.649$	$C_M = -0.101$
5000	$C_L = 0.0016$	$C_D = 0.0627$	$C_M = -0.001$	$C_L = 0.544$	$C_D = 0.574$	$C_M = -0.115$

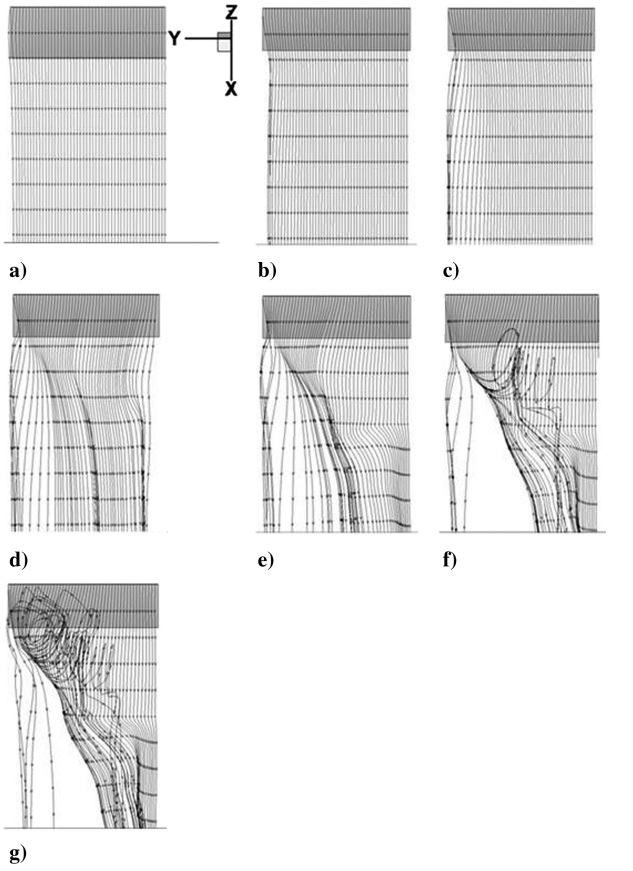

Fig. 14 Streamlines for cambered rectangular wing. The viewing direction is the same as in Fig. 13. Axis is for orientation purposes. Flow is from top to bottom, tip is left and root is right. Beginning at the top left, $\alpha = 0$, 10, 20, 30, 35, 40, and 45°. Vortex formation does not occur until $\alpha = 40°$.

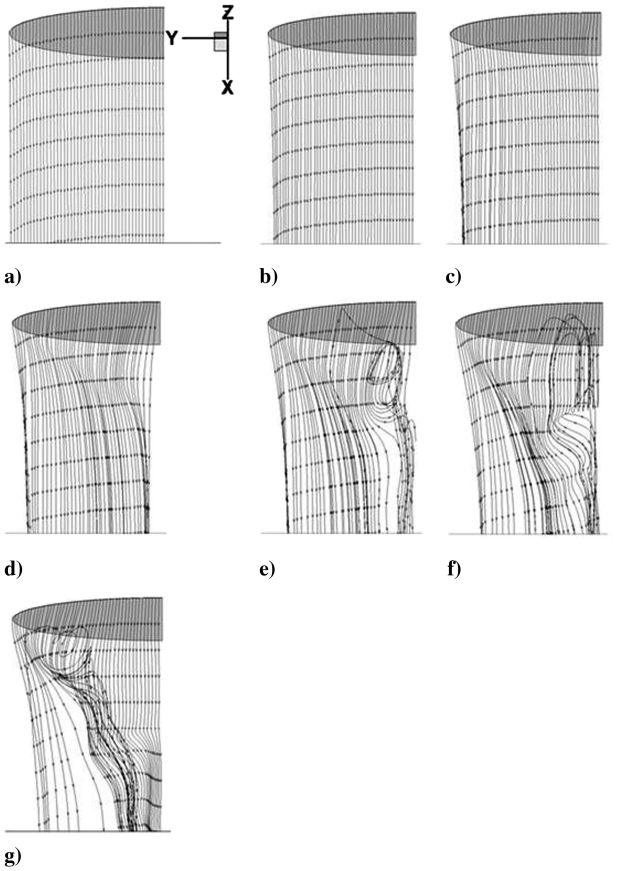

Fig. 15 Streamlines for noncambered semi-ellipse wing. The viewing direction is the same as in Fig. 13. Axis is for orientation purposes. Flow is from top to bottom, tip is left and root is right. Beginning at the top left, $\alpha = 0$, 10, 20, 30, 35, 40, and 45°. Vortex forms at root at $\alpha = 35$ and 40°, but vortex forms at tip at $\alpha = 45°$.

the leading edge near the root. Reverse flow is present on all wings and it forms a spiral vortex originating from the root, but only in the semi-ellipse wings. However, the behavior of the spiraling vortex is quite different from the above when the wing is undergoing complex motions such as flapping and pitching, as discussed by Isaac et al. [28]. This spanwise flow is significantly more predominant than on high-Re_c wings, on which well-defined tip vortices are formed. At low-Re_c, the freestream is not strong enough to cause the well-defined tip vortices; instead, the flow on the wing leeward surface becomes highly-three-dimensional, as indicated by the complex streamline pattern.

Kunz and Kroo [10] provided some numeric streamlines that show trailing-edge separation, which occurs at higher angles of attack at lower Reynolds numbers. Their Fig. 10 indicates a backward S-shaped feature, where flow near the trailing edge is initially in the freestream direction, reverses, and then returns to the freestream direction. This is quite like some of the stream traces along the symmetry plane in Fig. 18. Figure 19 shows streamlines for the noncambered rectangular wing at $\alpha = 45°$ for both $Re_c = 500$ and 5000. The vortex is present but much smaller at the higher Reynolds number, as anticipated. The same trend is also true for the reversed flow region.

C. Surface Stream Traces

Surface stream traces were prepared for both the suction and pressure surfaces of all four wings at all seven angles of attack. However, the pressure-surface stream traces are omitted because they are quite similar for all four wings and reveal only one trend: that trend is the tip vortex becoming increasingly powerful as angle of attack increases, as evidenced by stream traces curving toward the tip. Surface stream traces typically show much more complicated patterns than near-wake streamlines such as those present in Figs. 13–19. Comparisons between the two types of figures are made below, and corresponding features are explained. Flow features visible in one set of figures are reflected in the other set.

Figures 20–23 show suction-surface stream traces for the noncambered rectangular wing, cambered rectangular wing, noncambered semi-ellipse wing, and cambered semi-ellipse wing, respectively. Figure 24 shows surface stream traces for all four wings at $\alpha = 40°$. In Figs. 20–23, stream traces are parallel at $\alpha = 0°$, but start to curve near the tip at $\alpha = 10°$; this stream-trace deflection near the tip is more pronounced for the rectangular wings. This trend is also shown in Figs. 13–16, in which the tip vortex grows from $\alpha = 0$ to 10°. At and above $\alpha = 20°$, the patterns become more interesting. A small recirculation region is apparent at 20° near the root at the trailing edge for the semi-ellipse wings (Figs. 22c and 23c). This corresponds to the root vortex that develops on the semi-ellipse wings at higher angles of attack, as in Figs. 15e and 16e. The rectangular wings also show a swirling pattern, possibly indicative of vortices in the rootward half of the suction surface.

Separation at the leading edge is apparent on all wings at 30° with reattachment at 35° in the rectangular wings, as in Figs. 20e and 21e. However, in the semi-ellipse wings of Figs. 22d and 23d, there is no reattachment until 45°. Also apparent in all of the figures at 30° is a circular feature indicating a vortex near the tip, a likely unstable focus in the terminology of critical point theory, which is discussed later in this paper. Surface stream traces appear to converge at a point near the trailing edge at spanwise locations ranging between one-fourth and two-fifths span on all four wings at and above $\alpha = 35°$. This is particularly clear in Fig. 20f and can be seen by the stream traces to the right of the point of convergence veering to the right and the stream traces left of it veering to the left, indicative of a saddle point. This suggests spanwise variation of flow features. A second attractor

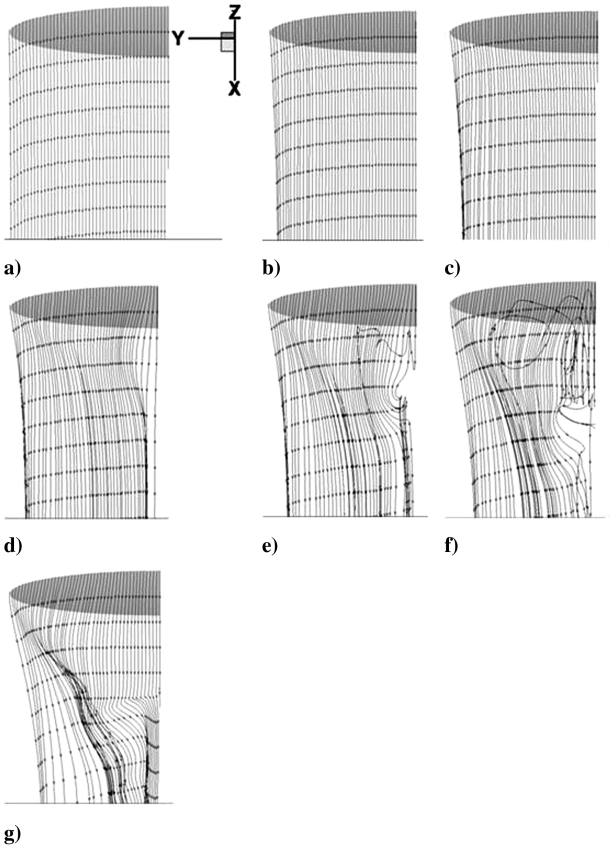

Fig. 16 Streamlines for cambered semi-ellipse wing. The viewing direction is the same as in Fig. 13. Axis is for orientation purposes. Flow is from top to bottom, tip is left and root is right. Beginning at the top left, $\alpha = 0$, 10, 20, 30, 35, 40, and 45°. Vortex does not form at $\alpha = 45°$, but does at $\alpha = 35$ and 40°.

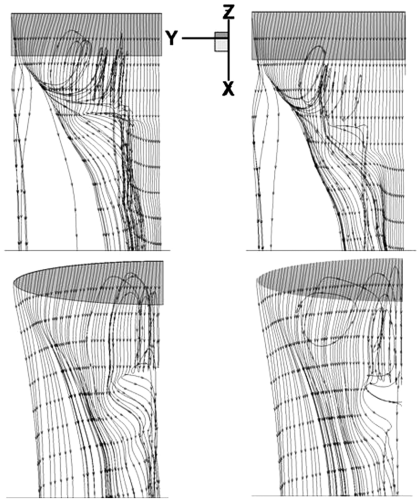

Fig. 17 Rectangular planform without camber and with camber (top) and semi-ellipse planform without camber and with camber (bottom); $\alpha = 40°$.

point, a saddle point, also exists for the semi-ellipse wings. Surface stream traces seem to originate from a point near the root at the trailing edge and spread out over a substantial portion of the surface of the wing for the 30–40° cases and is best shown in Fig. 23e. This is most likely attributable to the vortex that grows from the root on the semi-ellipse wings. A clear separation between this rootward region and the region closer to the tip where the streamlines are more nearly

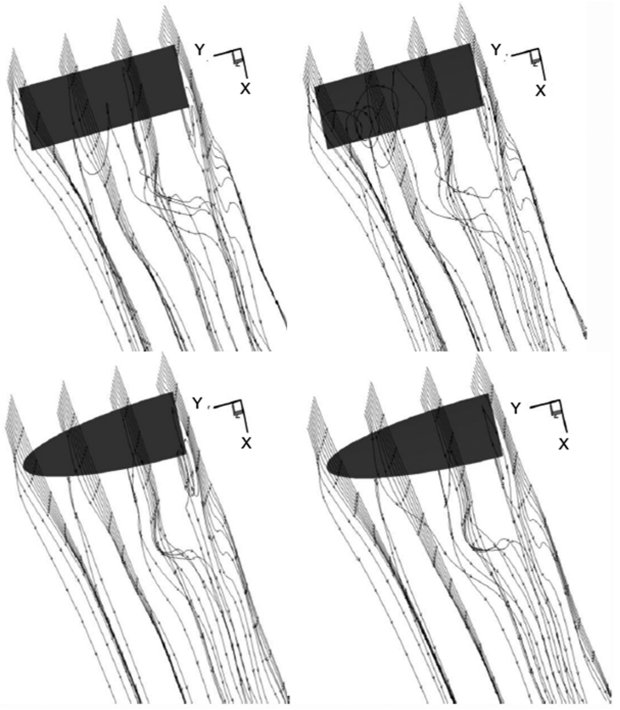

Fig. 18 Noncambered and cambered rectangle in top row, noncambered and cambered semi-ellipse in bottom row, at $\alpha = 45°$, showing the importance of wing planform on wake structure.

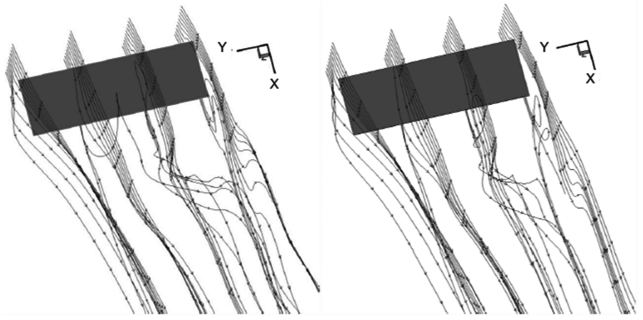

Fig. 19 Streamlines for $Re_c = 500$ (left) and $Re_c = 5000$ (right) with more reversed flow at the lower Reynolds number.

parallel can be easily seen. It is evident from Fig. 23 that the planform has more effect on surface stream-trace topology than does camber.

A comparison of the three-dimensional streamline patterns in Figs. 13–16 to the surface stream traces in Figs. 20–23 is also helpful to gain further understanding of the flowfield. Comparing Figs. 13c and 20c for the noncambered rectangular wing at $\alpha = 20°$ shows the

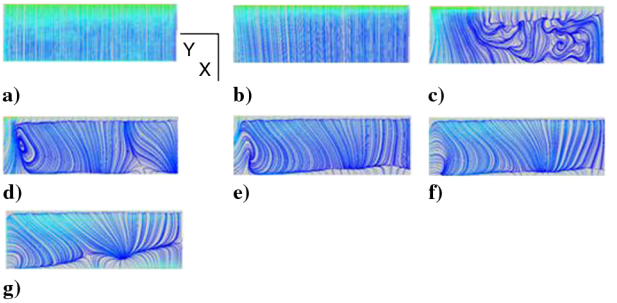

Fig. 20 Suction-surface stream traces for noncambered rectangular wing. Flow is from top to bottom, tip is left and root is right. Beginning at the top left, $\alpha = 0$, 20, 30, 35, 40, and 45°. Shades indicate shear stress. Note complicated pattern in part C.

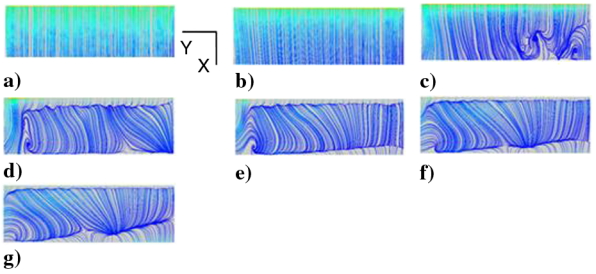

Fig. 21 Suction-surface stream traces for cambered rectangular wing. Flow is from top to bottom, tip is left and root is right. Beginning at the top left, $\alpha = 0$, 10, 20, 30, 35, 40, and 45°. Shades indicate shear stress. Image c is less complicated than in Figure 20, due to camber promoting attachment.

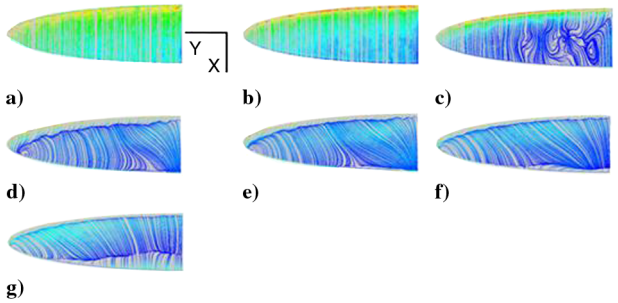

Fig. 22 Suction-surface stream traces for noncambered semi-ellipse wing. Flow is from top to bottom, tip is left and root is right. Beginning at the top left, $\alpha = 0$, 10, 20, 30, 35, 40, and 45°. Shades indicate shear stress. At higher angles of attack, the focus near the tip is smaller than for the rectangular planforms.

streamlines deflecting at the root and the tip (Fig. 13c) and the surface stream traces show a very complex vortex structure. A similar behavior is also apparent in Figs. 15c and 22c for noncambered semi-ellipse wings at $\alpha = 20°$. It appears that for the noncambered wings, $\alpha = 20°$ can be thought of as a transition angle of attack between the low-α attached flow regime and the high-α vortex-dominated flow regime. For the cambered wing at $\alpha = 20°$, the stream traces have fewer features, indicating the effect of surface curvature on establishing the vortex-dominated flowfield. Comparing the wake vortex structure in Figs. 13–16 and the surface vortex structure in Figs. 20–23, gives indications of vortex pairing. The vortices do not shed as in the two-dimensional cases with unsteady lift generation caused by vortex shedding; instead, they stay bound to the surface and have a complex structure depending on the angle of attack. The wake vortices do not coalesce into a well-defined tip vortex as is the case for high-Re_c wings. Instead, a wake vortex with a highly complex structure is visible. Its axis is curved, and it seems to break down fast, showing a strong dependence on the angle of attack.

A topological analysis of the surface streamline pattern using critical point theory is helpful to extract flow features [29–31]. To illustrate, the surface stream traces in Fig. 20e (noncambered, rectangular wing at $\alpha = 35°$) are traced in Fig. 25. Axis and wing orientation are the same in these figures. Two bifurcation lines, where the flow separates and reattaches, are present near the leading edge and the trailing edge. These are labeled BL^- and BL^+, respectively. Flow proceeds from the reattachment line to the separation line over much of the suction surface. A saddle point S is present on the bifurcation line BL^+. As mentioned earlier, an unstable focus, labeled F^-, from which streamlines spiral outward, can be seen near the wing tip. By examining the other surface stream traces shown in Figs. 20–23, the associated critical points can be extracted and sketched as in Fig. 25. Some of these stream traces are fairly complex, as in Figs. 20c and 22c for the noncambered wings at $\alpha = 20°$. In the neighborhood of $\alpha = 20°$, the flow seems to be transitioning to one in which the leading-edge vortex begins to form. However, for the two planforms with camber at the same angle of

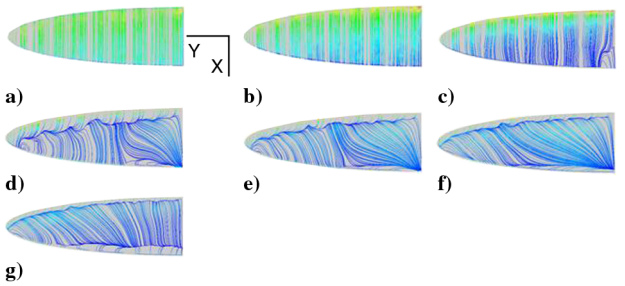

Fig. 23 Suction-surface stream traces for cambered semi-ellipse wing. Flow is from top to bottom, tip is left and root is right. Beginning at the top left, $\alpha = 0$, 10, 20, 30, 35, 40, and 45°. Shades indicate shear stress. A recirculation region is present at the root of the trailing edge in image c.

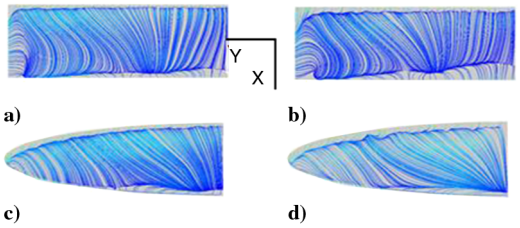

Fig. 24 Top row: rectangular wing without camber and with camber; bottom row: semi-ellipse wing without camber and with camber, $\alpha = 40°$. Changing the planform affects the flow features more than changing camber.

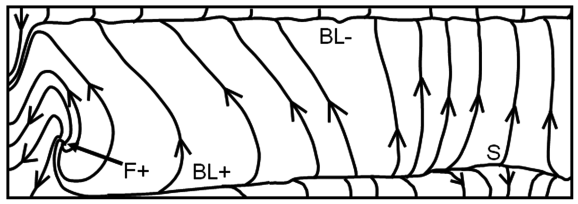

Fig. 25 Topological features of the surface flow extracted from the stream traces in Fig. 20e.

attack, the surface stream traces are not as complex, probably indicating that camber causes a smoother transition to vortex-dominated flow.

Based on the results, the following general observations can be made: At $\alpha = 20°$, there is no strong vortex on the leeward surface. The surface streamline pattern shows some waviness, probably due to the growing spanwise instability, which indicates a transition to vortex-dominated flow. This transition is also manifested in the drag polar (Fig. 7) and lift coefficient curve (Fig. 8), which shows a C_L maximum at $\alpha \approx 20°$. At $\alpha = 35°$ the flow pattern on the leeward side has become more complex. A wake vortex is present on the leeward surface, and the streamlines in this vortex are tightly packed. The vortex seems to break down somewhere between the tip and the root, the breakdown occurring closer to the tip at higher angles of attack. There is a slight spiraling of the vortex visible in the surface stream traces toward the wing tip, and the streamlines originating from this vortex merge with the tip vortex evolving into the wake vortex present in Figs. 13–16.

IV. Conclusions

The fixed-wing cases covered in the present study show that a tip vortex that strengthens with angle of attack is present over low-Reynolds-number ($Re_c = 500$) wings in the 0–45° angle-of-attack range. This tip vortex is the dominant flow feature and explains many aspects of the flow behavior. Lift peaks at an angle of attack slightly greater than 20° for all the wings and is attributable to a vortex-dominated flow at that angle of attack. Behavior above this angle of

attack varies differently for the rectangular wings and for the semi-ellipse wings, thus indicating the importance of planform shape. This behavior, generally a C_L decrease followed by a subsequent recovery, could be caused by tip vortices or the laminar separation bubble. Flow features include a tip vortex forcing streamlines rootward and creating highly-three-dimensional, low-velocity regions indicated by lower streamline density in the postprocessed results. This tip vortex forces the adjacent streamlines to curl into a spiral vortex on the rectangular wings at high angles of attack; the spiral vortex then breaks down, leading to the highly-three-dimensional low-velocity region. However, the semi-ellipse wings do not show such a clear tip vortex. Instead, a less coherent vortex is present toward the root (Figs. 15e, 15f, 16e, and 16f). Among the semi-ellipse-wing cases, only Fig. 15g has a clear tip vortex similar to those in the rectangular-wing cases. Surface stream traces indicate separation, recirculation, and reattachment at higher angles of attack. The flow patterns and C_L-α curves show significant departure from flow over wings at high Reynolds numbers, which have a well-defined tip vortex and stall angle of attack.

Further investigation is warranted of this important low-Reynolds-number flow regime for low-aspect-ratio wings with thin noncambered and cambered airfoil sections, with its applications to micro and nano air vehicles. A range of Reynolds numbers and aspect ratios need to be investigated to better understand this flow regime and wing geometries. A study of these wings undergoing a flapping or plunging and pitching motions would be of relevance to flapping-wing micro air vehicles. Ongoing research in our laboratory using computational fluid dynamics and experimental tools (flow visualization and particle image velocimetry) would help us gain further insight into insect, bird, and micro and nano air vehicle flight.

Acknowledgments

The authors wish to acknowledge the Missouri Space Grant for providing a fellowship to the lead author.

References

[1] Isaac, K. M., Shivaram, P., and DalBello, T., "Low Re, High a Aerodynamics with Controlled Wing Kinematics," AIAA Paper 2003-4019, Jun. 2003.

[2] Isaac, K. M., Colozza, A., and Rolwes, J., "Force Measurements on a Flapping and Pitching Wing at Low Reynolds Numbers," AIAA Paper 2006-0450, Jan. 2006.

[3] Isaac, K. M., Rolwes, J., and Colozza, A., "Unsteady Flow Features of a Flapping and Pitching Wing at Low Reynolds Number," AIAA Paper 2006-3145, Jun. 2006.

[4] McMasters, J. H., and Henderson, M. L., "Low-Speed Single-Element Airfoil Synthesis," NASA CP-2085, 1979, pp. 1–33.

[5] Lissaman, P. B. S., "Low-Reynolds-Number Airfoils," *Annual Review of Fluid Mechanics*, Vol. 15, 1983, pp. 223–239. doi:10.1146/annurev.fl.15.010183.001255

[6] Carmichael, B. H., "Low Reynolds Number Airfoil Survey," Vol. 1, NASA CR-165803, 1982.

[7] Selig, M. S., "The Design of Airfoils at Low Reynolds Numbers," AIAA Paper 85-0074, Jan. 1985.

[8] Laitone, E. V., "Aerodynamic Lift at Reynolds Numbers Below 7×10^4," *AIAA Journal*, Vol. 34, No. 9, Sep. 1996, pp. 1941–1942. doi:10.2514/3.13329

[9] Laitone, E. V., "Wind Tunnel Tests of Wings at Reynolds Numbers Below 70,000," *Experiments in Fluids*, Vol. 23, No. 5, Nov. 1997, pp. 405–409. doi:10.1007/s003480050128

[10] Kunz, P. J., and Kroo, I. M., "Analysis and Design of Airfoils for Use at Ultra-Low Reynolds Numbers," *Fixed and Flapping Wing Aerodynamics for Micro Air Vehicle Applications*, edited by T. Mueller, Vol. 195, Progress in Astronautics and Aeronautics, AIAA, Reston, VA, 2001, pp. 35–60.

[11] Mueller, T. J., "The Influence of Laminar Separation and Transition on Low Reynolds Number Airfoil Hysteresis," *Journal of Aircraft*, Vol. 22, No. 9, 1985, pp. 763–770. doi:10.2514/3.45199

[12] Selig, M. S., Guglielmo, J. J., Broeren, A. P., and Giguere, P., "Experiments on Airfoils at Low Reynolds Numbers," AIAA Paper 1996-0062, Jan. 1996.

[13] Biber, K., Ol, M. V., and Tilman, C. P., "Some Examples of Airfoil Design For Future Unmanned Air Vehicle Concepts," AIAA Paper 2004-1050, Jan. 2004.

[14] Hsiao, F.-B., Lin, C.-Y., Liu, Y.-C., Wand, D.-B., Wei, C.-Y., Chiang, C.-H., and Hsu, C.-C., "Investigation of Aerodynamic Performance on Low-Aspect Ratio Wings at Low Reynolds Numbers," AIAA Paper 2006-1266, Jan. 2006.

[15] Abtahi, A. A., and Marchman, J. F., "Aerodynamics of an Aspect Ratio 8 Wing at Low Reynolds Numbers," *Journal of Aircraft*, Vol. 22, No. 7, Jul. 1985, pp. 628–634. doi:10.2514/3.45176

[16] Viieru, D., Albertani, R., Shyy, W., and Ifju, P. G., "Effect of Tip Vortex on Wing Aerodynamics of Micro Air Vehicles," *Journal of Aircraft*, Vol. 42, No. 6, Nov. 2005, pp. 1530–1536. doi:10.2514/1.12805

[17] Kwon, K., and Park, S. O., "Aerodynamic Characteristics of an Elliptic Airfoil at Low Reynolds Number," *Journal of Aircraft*, Vol. 42, No. 6, Nov. 2005, pp. 1642–1644. doi:10.2514/1.16740

[18] Ricci, R., and Montelpare, S., "A Quantitative IR Thermographic Method to Study the Laminar Separation Bubble Phenomenon," *International Journal of Thermal Sciences*, Vol. 44, No. 8, Aug. 2005, pp. 709–719. doi:10.1016/j.ijthermalsci.2005.02.013

[19] Pelletier, A., and Mueller, T. J., "Low Reynolds Number Aerodynamics of Low-Aspect Ratio, Thin/Flat/Cambered-Plate Wings," *Journal of Aircraft*, Vol. 37, No. 5, Sep. 2000, pp. 825–832. doi:10.2514/2.2676

[20] Kaplan, S. M., Altman, A., and Ol, M., "Wake Vorticity Measurements for Low Aspect Ratio Wings at Low Reynolds Number," *Journal of Aircraft*, Vol. 44, No. 1, Jan. 2007, pp. 241–251. doi:10.2514/1.23096

[21] Cosyn, P., and Vierendeels, J., "Numerical Investigation of Low Aspect Ratio Wings at Low Reynolds Numbers," *Journal of Aircraft*, Vol. 43, No. 3, May 2006, pp. 713–722. doi:10.2514/1.16991

[22] Swanson, T., and Isaac, K. M., "Aerodynamics of Flapping and Plunging Wings Using Particle Image Velocimetry Measurements," AIAA Paper 2009-1271, Jan. 2009.

[23] FLUENT, Software Package, Ver. 6.3, Fluent, Inc., Lebanon, NH, 2002.

[24] Young, J., Lai, J. C. S., and Germain, C., "Simulation and Parameter Variation of Flapping-Wing Motion Based on Dragonfly Hovering," *AIAA Journal*, Vol. 46, No. 4, Apr. 2008, pp. 918–924. doi:10.2514/1.31610

[25] White, F., *Viscous Fluid Flow*, 3rd ed., McGraw–Hill, New York, 2006.

[26] Sunada, S., Yasuda, T., Yasuda, K., and Kawachi, K., "Comparison of Wing Characteristics at an Ultralow Reynolds Number," *Journal of Aircraft*, Vol. 39, No. 2, Mar. 2002, pp. 331–338. doi:10.2514/2.2931

[27] Swanson, T., and Isaac, K. M., "Low *Re*, High Alpha Wing Aerodynamics for Micro Air Vehicle Applications," AIAA Paper 2008-0421, Jan. 2008.

[28] Isaac, K. M., Rolwes, J., and Colozza, T., "Aerodynamics of a Flapping and Pitching Wing Using Simulations and Experiments," *AIAA Journal*, Vol. 46, No. 6, Jun. 2008, pp. 1505–1515. doi:10.2514/1.32846

[29] Tobak, M., and Peake, D. J., "Topology of Three-Dimensional Separated Flows," *Annual Review of Fluid Mechanics*, Vol. 14, 1982, pp. 61–85. doi:10.1146/annurev.fl.14.010182.000425

[30] Perry, A. E., and Chong, M. S., "A Description of Eddying Motions and Flow Patterns Using Critical Point Concepts," *Annual Review of Fluid Mechanics*, Vol. 19, 1987, pp. 125–155. doi:10.1146/annurev.fl.19.010187.001013

[31] Yavuz, M. M., and Rockwell, D., "Control of Flow Structure on Delta Wing with Steady Trailing-Edge Blowing," *AIAA Journal*, Vol. 44, No. 3, Mar. 2006, pp. 493–501. doi:10.2514/1.16444